Solar Phys (2007) 240: 315–330
DOI 10.1007/s11207-007-0285-8

# Coronal Holes and Solar Wind High-Speed Streams: I. Forecasting the Solar Wind Parameters

**Bojan Vršnak · Manuela Temmer · Astrid M. Veronig**

Received: 5 August 2006 / Accepted: 23 December 2006 /
Published online: 27 February 2007


**Abstract** We analyze the relationship between the coronal hole (CH) area/position and physical characteristics of the associated corotating high-speed stream (HSS) in the solar wind at 1 AU. For the analysis we utilize the data in the period DOY 25 – 125 of 2005, characterized by a very low coronal mass ejection (CME) activity. Distinct correlations between the daily averaged CH parameters and the solar wind characteristics are found, which allows us to forecast the solar wind velocity $v$, proton temperature $T$, proton density $n$, and magnetic field strength $B$, several days in advance in periods of low CME activity. The forecast is based on monitoring fractional areas $A$, covered by CHs in the meridional slices embracing the central meridian distance ranges $[-40°, -20°]$, $[-10°, 10°]$, and $[20°, 40°]$. On average, the peaks in the daily values of $n$, $B$, $T$, and $v$ appear delayed by 1, 2, 3, and 4 days, respectively, after the area $A$ attains its maximum in the central-meridian slice. The peak values of the solar wind parameters are correlated to the peak values of $A$, which provides also forecasting of the peak values of $n$, $B$, $T$, and $v$. The most accurate prediction can be obtained for the solar wind velocity, for which the average relative difference between the calculated and the observed peak values amounts to $\overline{|\delta|} \approx 10\%$. The forecast reliability is somewhat lower in the case of $T$, $B$, and $n$ ($\overline{|\delta|} \approx 20$, 30, and 40%, respectively). The space weather implications are discussed, including the perspectives for advancing the real-time calculation of the Sun – Earth transit times of coronal mass ejections and interplanetary shocks, by including more realistic real-time estimates of the solar wind characteristics.

B. Vršnak (✉) · M. Temmer
Hvar Observatory, Faculty of Geodesy, Zagreb, Croatia
e-mail: bvrsnak@geodet.geof.hr

M. Temmer
e-mail: mat@igam.uni-graz.at

A.M. Veronig
IGAM/Institute of Physics, University of Graz, Graz, Austria
e-mail: asv@igam.uni-graz.at

## 1. Introduction

Coronal holes (CHs) are sources of fast solar wind, predominantly associated with solar polar regions (Gosling and Pizzo, 1999). Occasionally, CHs appear also at low latitudes, forming high-speed streams (HSSs) in the region otherwise characterized by the slow solar wind (for a review see, *e.g.*, Schwenn, 2006; Tsurutani *et al.*, 2006, and references therein). The resulting solar/interplanetary structures are often stable over longer periods, surviving for several solar rotations and creating a periodic pattern in the *in situ* solar wind measurements (so-called corotating streams).

The interaction of a fast stream and the upstream slow solar wind compresses the plasma and magnetic field at the boundary, causing a density and magnetic field enhancement in the upstream slow wind. In contrast, in the fast solar wind region, the kinetic energy is transformed to thermal energy, causing plasma heating and expansion (*e.g.*, Alves, Echer, and Gonzalez, 2006, and references therein). If the CH – HSS structure is stable over a longer period of time, the pattern of the interaction region is repeated each solar rotation, which is called a corotating interaction region (CIR).

From the space weather aspect, the CIR/HSS phenomenon is important for several reasons. Owing to the high plasma velocity, enhanced magnetic field, and Alfvén-wave-associated magnetic field fluctuations, CIR – HSS structures cause long-living geomagnetic storms, usually lasting for several days (*e.g.*, Burlaga and Lepping, 1977; Tsurutani and Gonzalez, 1987; see also Borovsky and Denton, 2006; Xie *et al.*, 2006, and references therein). Their strength rarely reaches $Dst = -100$ nT (where the *Dst* index measures the intensity of the geomagnetic disturbance; for details see http://swdcwww.kugi.kyoto-u.ac.jp/dst2/onDstindex.html); *i.e.*, they are generally weaker than severe storms caused by interplanetary coronal mass ejections (ICMEs). However, their overall contribution to geomagnetic activity is comparable to, if not even more important than, that of ICMEs (Tsurutani *et al.*, 2006). In particular, CIR – HSSs play a dominant role in geomagnetic activity during the declining phase of the solar cycle (*e.g.*, Alves, Echer, and Gonzalez, 2006; Tsurutani *et al.*, 2006, and references therein).

Another important space weather aspect is the interaction of ICMEs with HSSs. First, such an interaction can intensify and/or prolong the ICME-associated geomagnetic storms because of the compression of the internal field of the ejection in its rear part (Webb *et al.*, 2000; Dal Lago *et al.*, 2002, 2006; Xie *et al.*, 2006). Second, HSSs can significantly affect the dynamics of transient interplanetary phenomena; *i.e.*, HSS effects are important for calculating the Sun – Earth transit times of ICMEs and shocks (*e.g.*, Dryer *et al.*, 2004; Odstrčil, Riley, and Zhao, 2004; Odstrčil, Pizzo, and Arge, 2005; Smith, Dryer, and Fry, 2006; Dal Lago *et al.*, 2006; Tappin, 2006, and references therein).

Since CIR – HSSs are associated with CHs, which are relatively stable solar structures (in contrast to the unpredictable CME activity), there should be a way to forecast quantitatively the CIR – HSS effects at 1 AU by observing low-latitude CHs after they appear at the eastern limb of the Sun. That can be done either by applying various forms of MHD modeling (*e.g.*, Arge and Pizzo, 2000; Arge *et al.*, 2004; Detman *et al.*, 2006, and references therein) or by directly utilizing various empirical relationships between the size/position of low-latitude CHs and solar wind parameters measured at 1 AU (*e.g.*, Robbins, Henney, and Harvey, 2006).

Recently, Robbins, Henney, and Harvey (2006) performed a detailed analysis of the solar wind data and areas of CHs measured in the Kitt Peak He I 1083 nm spectroheliograms to relate CH data with the semi-daily averages of the solar wind velocity. They found a poor correlation of the CH areas and the solar wind speed in the rising phase and maximum of

the solar activity cycle, whereas the best correlation was found in the declining phase of the solar cycle.

In this paper we perform a quantitative analysis of the relationship between the area/location of CHs and various characteristics of the associated CIR – HSSs, whereas in the follow-up paper (Vršnak, Temmer, and Veronig, 2007), we extend the analysis to the CH – HSS-related geomagnetic disturbances. We focus on the data in the first half of 2005, settled in the declining phase of the solar cycle 23, and being analogous to the first part of the interval denoted as Bin 2 in Figure 4 of Robbins, Henney, and Harvey (2006). The aim of the paper is to provide a simple forecasting tool, which could enable a fully automatic prediction of the basic parameters of HSSs (flow velocity, density, temperature, and magnetic field strength) several days in advance, for periods of low CME activity. Furthermore, predictions of the spatial and temporal evolution of the ambient solar wind speed and density may be applied to the kinematical modeling of the Sun – Earth transit times of CMEs (*e.g.*, Vršnak and Gopalswamy, 2002) and/or interplanetary shocks (*cf.* Dryer *et al.*, 2004, and references therein).

The analysis is based on the identification of CHs from daily soft X-ray (SXR) solar images. There are several reasons to employ the SXR data and perform an analysis complementary to that reported by Robbins, Henney, and Harvey (2006). The most important one is that identification of CHs and estimation of their areas is quite intricate, and the outcome depends strongly on the observing wavelength (*e.g.*, de Toma and Arge, 2005; Shen *et al.*, 2006). Consequently, it is important to check how much the performances of the forecasting procedure depend on the observational technique by which CH areas are estimated. For example, an automatic identification of CHs in the EUV spectral range is complicated by presence of filaments and transient dimmings (*e.g.*, Shen *et al.*, 2006). Furthermore, the methods based on EUV (and SXR) data are subject to the line-of-sight effects (*i.e.*, bright coronal features intercepting the line of sight and obscuring the CHs). On the other hand, the CH identification based on He I 1083 nm spectroheliograms requires comparison with the magnetograph data, so it is difficult to perform an automatic procedure on a real-time basis. Moreover, the correspondence between open magnetic structures and observed coronal holes is still not settled (*e.g.*, Jones, 2005).

## 2. Observations

### 2.1. The Data Set

The solar wind and interplanetary magnetic field data utilized in the present study were taken from the Solar Wind Electron, Proton, and Alpha Monitor (SWEPAM; McComas *et al.*, 1998) and the magnetometer instrument (MAG; Smith *et al.*, 1998) onboard the Advanced Composition Explorer (ACE; Stone *et al.*, 1998). The SWEPAM measures the solar wind plasma electron and ion fluxes as functions of direction and energy, which provides detailed knowledge of the solar wind conditions. For our purpose we used level-2 data of daily averages of the proton density $n$ [cm$^{-3}$], proton temperature $T$ [K], and proton speed (solar wind bulk speed) $v$ [km s$^{-1}$]. The MAG measures continuously the direction and magnitude of the local interplanetary magnetic field. Level-2 data of daily averages of the magnetic field magnitude $B$ [nT] were used. The SWEPAM and MAG data were linearly interpolated for days with bad or missing data.

Daily solar coronal hole areas were determined from soft X-ray images acquired by the Soft X-ray Imager (SXI; Hill *et al.*, 2005; Pizzo *et al.*, 2005) onboard the GOES-12

spacecraft. SXI observes the Sun in six different filter positions with a spatial resolution of 5 arcsec/pixel and is primarily sensitive to coronal plasma in the temperature range $\approx 1-10$ MK. In the present study we used the SXI coronal hole image product (level-2 files), which became available after the loss of the Open Filter position and performance degradation of the SXI instrument in 2003. The level-2 files are created from stacking 12 hours of solar-rotation-corrected level-1 (calibrated) images taken through the SXI Thin Polyimide (PTHN) filter with 3 s integration, substantially improving the signal-to-noise ratio with respect to individual images (Hill *et al.*, 2005; see also http://sxi.ngdc.noaa.gov/).

The level of CME activity was checked in the *CME Online Catalogue* (http://cdaw.gsfc.nasa.gov/CME_list/; Yashiro *et al.*, 2004), which is based on the data gained by the Large Angle and Spectrometric Coronagraph (LASCO; Brueckner *et al.*, 1995) onboard the Solar and Heliospheric Observatory (SOHO). To consider only the potentially geoeffective CMEs, we focused on full halo (F) and partial halo (P) CMEs that were earthward directed, *i.e.*, identified as front-side events. Partly, this detailed information is given in the Halo CME archive (http://lasco-www.nrl.navy.mil/halocme.html; *cf.* St. Cyr *et al.*, 2000, and Yashiro *et al.*, 2004). For CME events with no entry in this archive we checked flare list events and decided according to the activity level and roughly contemporaneous appearances of flares whether the CME was front- or back-sided.

In this paper we focus on a period of low CME activity during 2005. Since SXI entered safe hold mode from 11 September until 20 October 2005, we constrained the analysis to 1 January until 11 September 2005. During this period, the main emphasis is laid on the time range 25 January until 5 May, *i.e.*, day of year (DOY) 25 – 125, where the solar CME activity was particularly low.

### 2.2. CH Measurements

Each day, four SXI coronal images (level-2 files) are provided around 1, 7, 13, and 19 UT (these nominal times refer to the mid time of the 12-hour level-1 image summation). For our purpose we used one SXI coronal image per day taken around 13 UT. In measuring the CH areas we applied a fixed threshold to the calibrated SXI coronal hole images of 0.15 DN $s^{-1}$. All pixels below this threshold (identified as coronal hole pixels) within a specified region of the visible solar disk were summed and divided by the total number of pixels of the considered region in order to calculate the fractional area $A$ covered by CHs.

Specifically, we determined for each day the fractional CH area $A$ in three meridional "slices" embracing the central-meridian distance ranges $[-40, -20]$, $[-10, 10]$, and $[20, 40]$ degrees. The Eastern, central-meridian, and Western slice are hereinafter denoted as E slice, M slice, and W slice, respectively. Furthermore, we applied two latitude-window options, considering (i) the full latitudinal range, *i.e.*, $[-90, 90]$ degrees, and (ii) the latitudinal range restricted to $[-30, 30]$ degrees, in order to inspect the relative contribution of equatorial and high-latitude coronal holes. The top panel of Figure 1 illustrates the determination of CH areas in the M slice for three SXI images of the series.

Finally, since the aim of the paper is to provide a forecasting tool as simple as possible, we also performed the measurements in a simple plane-of-sky North – South oriented bin embracing the East – West range $x = [-200, 200]$ arcsec (hereinafter central bin, or C bin). Again we checked the relative contribution of low-latitude and polar CHs, by considering the whole bin and restricting its North – South range to $[-700, 700]$ and $[-500, 500]$ arcsec (roughly corresponding to latitudes $\pm 45°$ and $\pm 30°$). The derived series of daily values of $A$ were adjusted from $\approx$13 UT to 12:00 UT by a simple linear interpolation in order to be compatible with the ACE daily values of solar wind parameters.

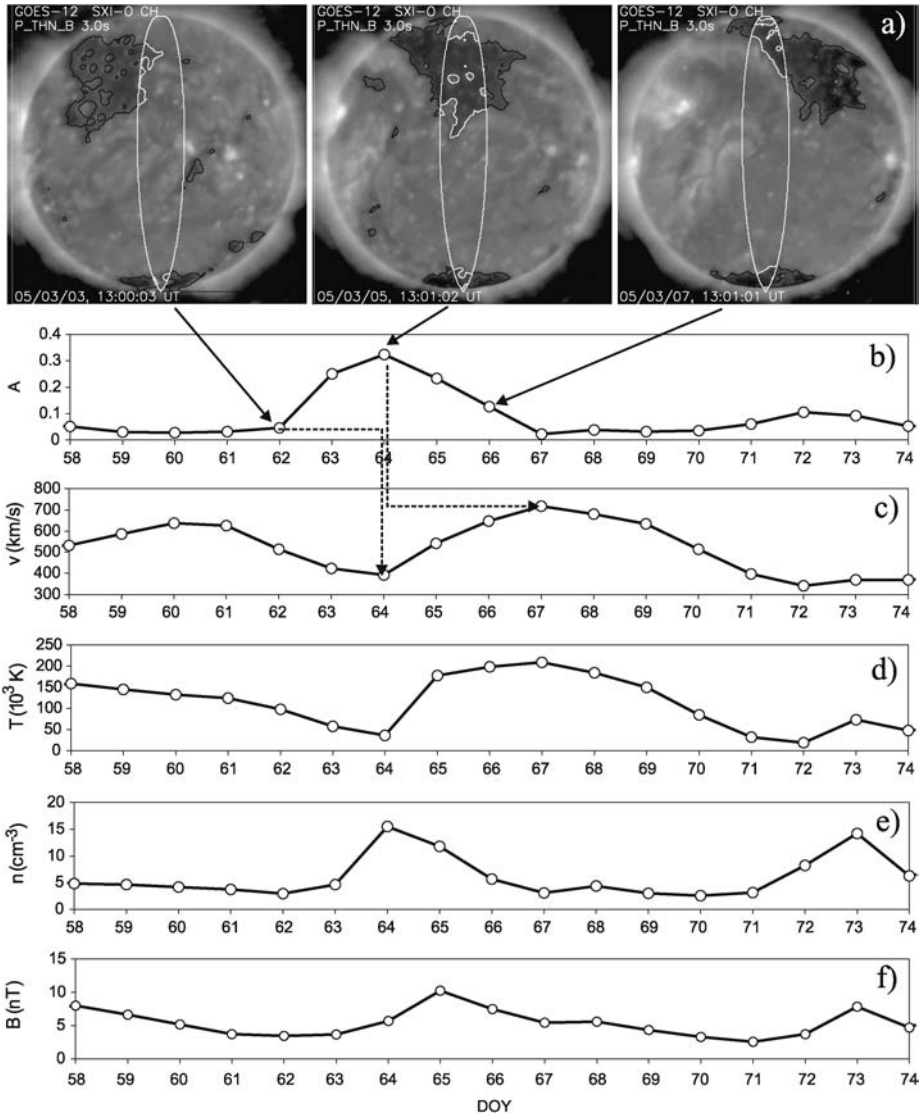


**Figure 1** a) Transition of a large coronal hole over the solar disc recorded by GOES-SXI. The considered meridional slice $[-10°, 10°]$ is outlined in white. The derived coronal hole boundaries inside the slice are also outlined in white. The coronal hole boundaries outside the slice are indicated in black. b) Daily measurements of the CH fractional area $A$ in the M slice ($[-10°, 10°]$, depicted in a). c) – f) ACE daily averages of the solar wind parameters: flow velocity $v$, proton temperature $T$, density $n$, and magnetic field strength $B$. The $x$-axis represents DOY for 2005. Bold arrows connect images with the corresponding CH measurements. Dashed lines outline the time lag between a CH measurement and the corresponding 1 AU effect.

Figure 1 illustrates a typical situation in the period we consider. As the large CH in the northern hemisphere rotates over the measuring slice located at the central meridian (M slice), it creates a rise in the $A_{\mathrm{M}}$ value starting at DOY 62, attaining maximum at DOY 64, and returning to the background level at DOY 67. The ACE measurements of the solar

wind speed, density, temperature, and magnetic field show an increase associated with the CH transition. The solar wind velocity starts increasing in this case approximately simultaneously with the peak of $A_{\rm M}$ (middle panel of Figure 1a and DOY 64 in Figure 1b), *i.e.*, two days after the leading edge of the CH approached the border of the M slice (left panel of Figure 1a and DOY 62 in Figure 1b). The ACE daily averages reflect a typical high-speed stream behavior: First we recognize the density and the magnetic field bump, whereas the temperature attains a maximum after the density and magnetic field bump and shows a time profile similar to the velocity profile. In this particular case, the stream velocity peaks three days after the maximum of the $A_{\rm M}(t)$ curve.

### 2.3. Relationship Between CHs and Solar Wind Parameters

In Figure 2 we show the data for the whole period analyzed. The coronal hole and solar wind data show a periodic pattern characterized by a 9-day period, particularly in the interval DOY 25 – 125.[1] Such a behavior is governed by three persistent low-latitude CHs, mutually separated in longitude by $\approx 120^\circ$. Such a configuration of CHs and related HSSs, created 11 peaks in $A(t)$ and the solar wind data in the DOY 25 – 125 interval. The peaks are marked by vertical lines in Figure 2, which are "broken" in such a manner to account for the delay between the solar wind speed and the CH passage across the central meridian.

For the eleven peaks, we present in Table 1 the DOY and maximum value of $A_{\rm M}$ (columns 2 and 3) and the corresponding peak values of $n$, $B$, $T$, and $v$ (columns 5, 7, 9, and 11,

**Table 1** For the eleven peaks during the time interval DOY 25 – 125, the fractional CH area measured in the M slice ($A_{\rm M}$), the corresponding peak values for the solar wind proton density $n$, magnetic field strength $B$, proton temperature $T$, and bulk speed $v$, as well as their delays $\Delta t_{n,B,T,v}$ with respect to $A_{\rm M}$, are given. In the last two rows, the average values and the standard deviations are displayed.

| Peak | DOY 2005 | $A_{\rm M}$ | $\Delta t_n$ [days] | $n$ [cm$^{-3}$] | $\Delta t_B$ [days] | $B$ [nT] | $\Delta t_T$ [days] | $T$ [$10^3$ K] | $\Delta t_v$ [days] | $v$ [km s$^{-1}$] |
|---|---|---|---|---|---|---|---|---|---|---|
| 1 | 27 | 0.24 | 2 | 11.6 | 2 | 13.3 | 2 | 150 | 4 | 605 |
| 2 | 37 | 0.18 | 1 | 11.4 | 2 | 11.7 | 2 | 225 | 3 | 707 |
| 3 | 46 | 0.10 | 1 | 10.6 | 3 | 10.3 | 4 | 100 | 3 | 509 |
| 4 | 55 | 0.34 | −1 | 10.7 | −1 | 10.8 | 3 | 159 | 5 | 638 |
| 5 | 64 | 0.32 | 0 | 15.5 | 1 | 10.3 | 3 | 209 | 3 | 717 |
| 6 | 73 | 0.09 | 0 | 14.2 | 2 | 8.1 | 3 | 86 | 4 | 406 |
| 7 | 82 | 0.37 | 1 | 9.7 | 2 | 10.7 | 2 | 244 | 3 | 651 |
| 8 | 91 | 0.32 | 2 | 15.6 | 3 | 10.0 | 3 | 191 | 4 | 617 |
| 9 | 99 | 0.32 | | | 3 | 9.7 | 4 | 214 | 4 | 574 |
| 10 | 110 | 0.30 | −1 | 34.7 | 0 | 8.6 | 0 | 202 | 4 | 546 |
| 11 | 118 | 0.36 | 1 | 21.9 | 2 | 9.8 | 3 | 287 | 3 | 640 |
| Average | | 0.27 | 0.60 | 15.6 | 1.7 | 10.3 | 2.6 | 188 | 3.6 | 601 |
| Standard deviation | | 0.10 | 1.07 | 7.6 | 1.3 | 1.4 | 1.1 | 60 | 0.7 | 90 |

[1]The same periodicity could be recognized intermittently in the complete set of the $v$, $n$, $T$, and $B$ ACE data, starting from February 1998. However, except for the 2005 DOY 25 – 125 interval, the solar wind was generally significantly affected by ICMEs.

respectively). In columns 4, 6, 8, and 10, the lags between peaks of the solar wind parameters and the $A_M$ peaks are shown. From this we can also derive the interrelation between the analyzed solar wind parameters themselves. From Table 1 we can see that the peak values of the fractional CH areas cover the range from ≈0.1 to ≈0.4. The density peaks are generally larger than 10 $cm^{-3}$, whereas the magnetic field peaks group around 10 nT. The temperature and the velocity maxima are found in the range (90 – 280) $\times 10^3$ K and ≈400 – 700 $km\,s^{-1}$, respectively.

## 3. Basic Features and Correlations

### 3.1. Cross-Correlations

Inspecting Table 1, we find that the density peaks occur roughly contemporaneously with the $A_M$ peaks. However, they may appear one day in advance and up to two days delayed. On average, the magnetic field strength reaches its maximum one day after the density. The temperature and velocity are increased over extended periods, attaining broad maxima most often 3 – 4 days after the $A_M$ maximum. The velocity peaks most often after the temperature maximum. During the period of increased velocity, the density and magnetic field strength decreased (see also Figure 2). Such a pattern of daily values is consistent with CIR – HSS structures observed at higher time resolution (see, *e.g.*, Figure 3 of Borovsky and Steinberg, 2006, or Figure 5 of Tsurutani *et al.*, 2006). The "early" appearance of the density peak is caused by its close relation to the leading edge of the CH – HSS structure and the propagation of the perturbation into the HSS-upstream slow-wind region. The delays of the velocity peaks after the $A_M$ maxima are consistent with that found by Robbins, Henney, and Harvey (2006).

In the following, we quantify the time delays by applying a cross-correlation analysis. In Figure 3 we show the cross-correlation functions for the CH area in the M slice ($A_M$) versus $v$, $T$, $n$, and $B$, respectively. We present only the results for the M-slice measurements of $A$, in the period DOY 25 – 125. The cross-correlation is calculated up to a time lag of ±20 days.

The velocity and the temperature show higher correlation coefficients than the density and the magnetic field. The time lags for $A - v$ $A - T$, $A - B$, and $A - n$ correlations are 4, 3, 2, and 1 days, respectively. These delays will be utilized in the forecasting procedure, which is presented in Section 4. Note that the 4-day lag between the peak in solar wind speed and the passage of the coronal hole across the central meridian (peak of $A_M$) corresponds to the footpoint location of the field lines connected to the Earth at 50 – 60° West.

In Figure 4, the cross-correlation functions for various combinations of the solar wind parameters are presented. The relative time lags are consistent with the time lags found in Figure 3. In addition, the $n - v$ function reveals a density depletion at around the time of the velocity peak (negative correlation coefficient dip in the cross-correlation function around $t = 0$). Figures 3 and 4 show that the peaks in daily values of the solar wind parameters appear in the succession $n \rightarrow B \rightarrow T \rightarrow v$ and are mutually lagged by about one day.

### 3.2. Time-Lagged Correlations

Figure 3 clearly shows that there is a distinct relationship between the area/position of coronal holes and the solar wind parameters. The calculated time lags in Figures 3 and 4 reflect

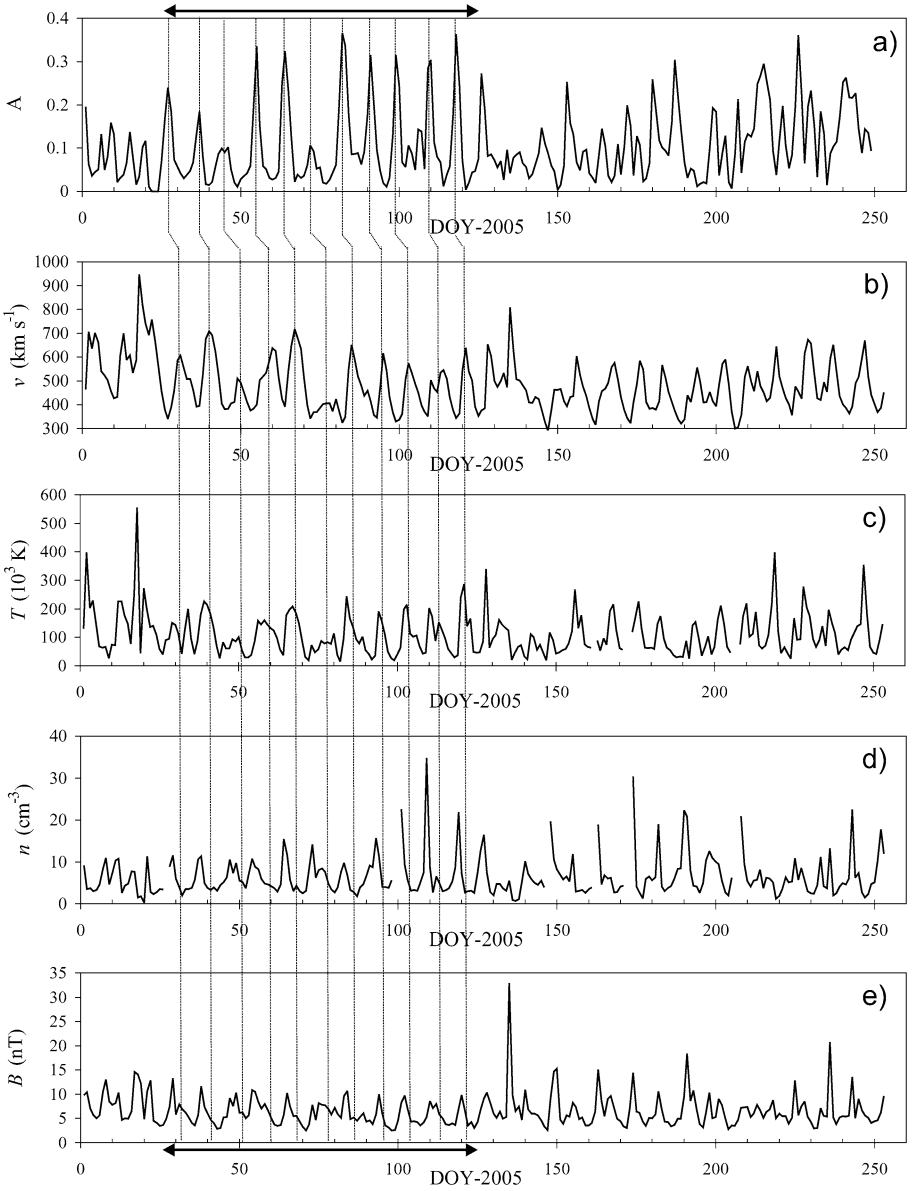


**Figure 2** The data in the analyzed period: a) SXI coronal hole area in the M slice; b) – e) solar wind parameters: flow velocity, proton temperature, density, and the magnetic field strength. The $x$-axis represents DOY for 2005. Peaks in the coronal hole data in the period DOY 25 – 125 (horizontal bold double-sided arrow) are related to the corresponding solar wind features by vertical lines. The displacement of the vertical lines (from a) to b)) indicates the delay between peaks in $A$ and $v$.

the pattern illustrated in Figure 1: First the density and the magnetic field bumps appear, the latter being delayed by 1 day. Then, the temperature attains a maximum during the decrease of $B$ and $n$. Finally, the velocity attains a maximum around, or one day after, the temperature

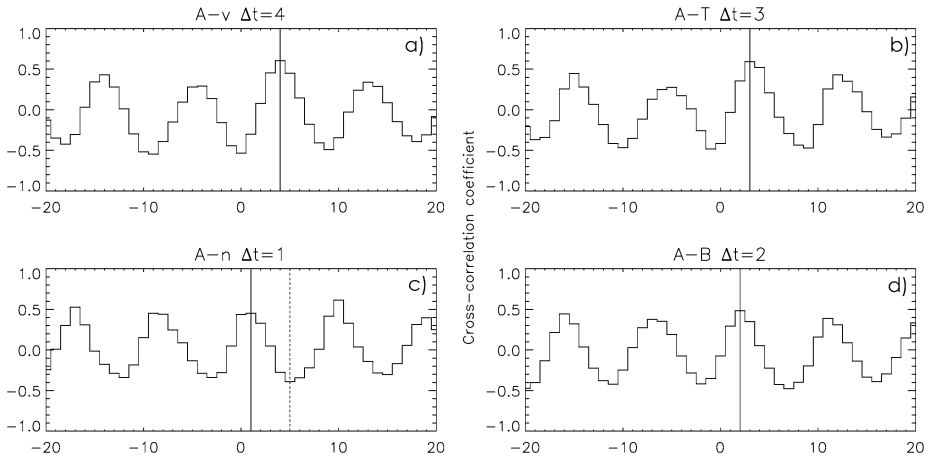


**Figure 3** Cross-correlation coefficients derived from the daily values of the coronal hole areas $A$ in the central-meridian slice and the ACE daily values for a) solar wind velocity $v$; b) proton temperature $T$; c) density $n$; and d) magnetic field $B$. The cross-correlation function was calculated up to a time lag of $\pm 20$ days. Only the data in the period DOY 25 – 125 are considered. The time lags $\Delta t$ used for forecasting are marked by vertical lines and written in the graph headers.

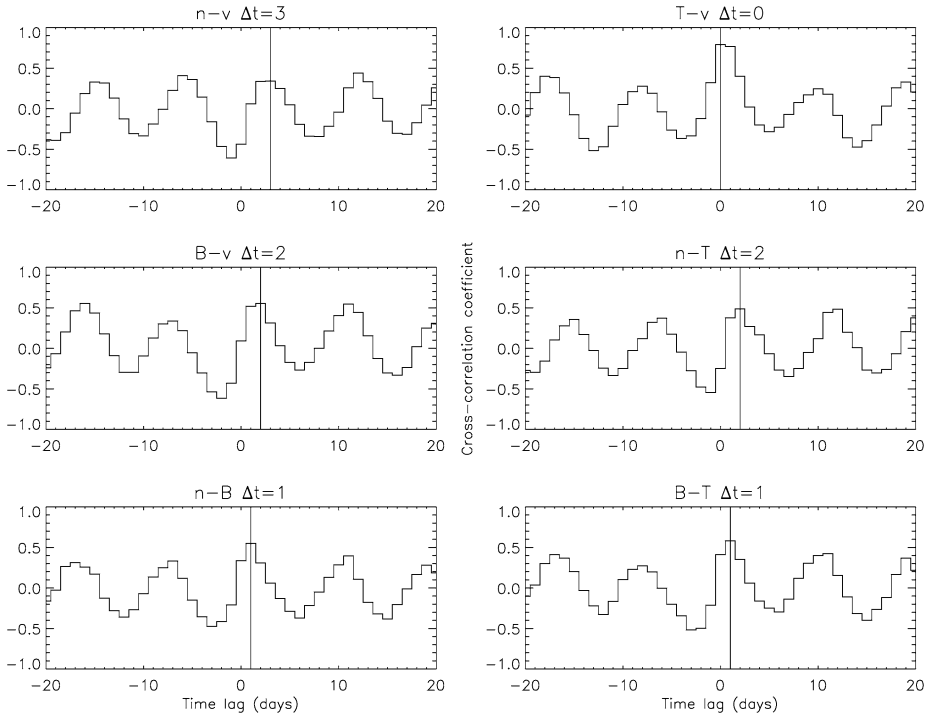


**Figure 4** Cross-correlations between solar wind parameters.

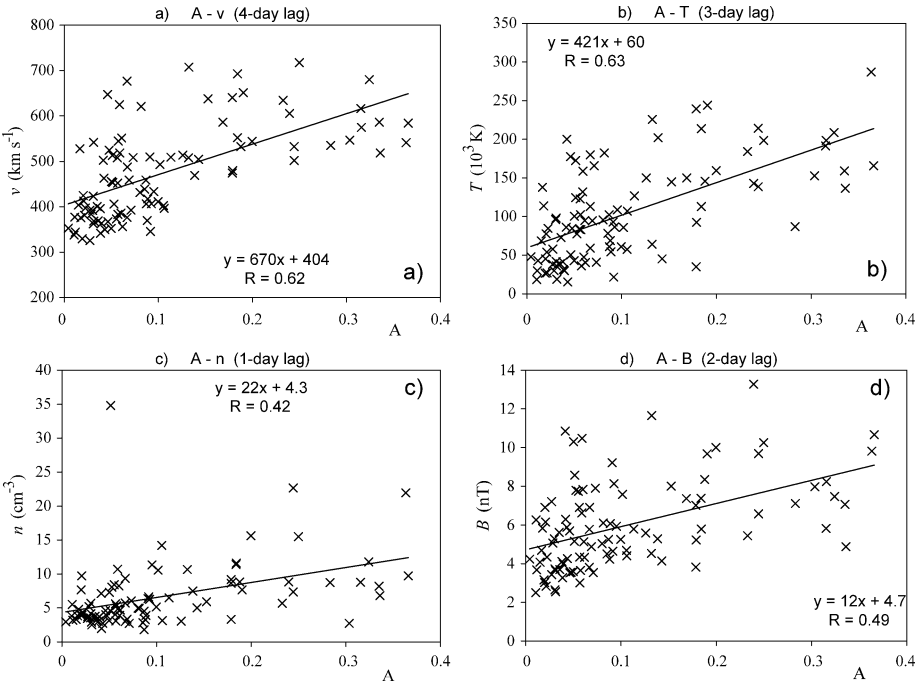


**Figure 5** Time-lagged correlations of the coronal hole areas in the central-meridian slice and a) solar wind velocity $v$; b) proton temperature $T$; c) density $n$; and d) magnetic field $B$. The applied time lags are indicated in the graph headers. Only the data in the period DOY = 25 – 125 are shown. The least-squares fits, together with the corresponding correlation coefficients, are indicated in the insets.

maximum, roughly at the time of a broad $n$ and $B$ minimum (for the anti-correlation of $n$ and $v$, as well as $B$ and $v$ see also Figure 2).

The solar wind parameters are temporally aligned with the CH areas by utilizing the time lags found in the previous section. Figure 5 shows the relationship between the time-lagged solar wind parameters and the CH areas $A_{\rm M}$, from which we obtain distinct correlations for $v(A)$ and $T(A)$ and somewhat weaker correlations for $n(A)$ and $B(A)$. Nevertheless, the statistical F-test significance of all correlations is larger than 99%. The linear least-squares fits and the corresponding correlation coefficients $R$ are provided in the insets of Figure 5.

Bearing in mind the well-known anti-correlation between the solar wind density $n$ and velocity $v$ (see, *e.g.*, Figure 3 of Gosling and Pizzo, 1999), one could also consider the anti-correlation of $n$ and $A$, lagged by 5 days (see dashed line in Figure 3c). In that case the anti-correlation with a 5-day lag could be expressed as $n\ [\mathrm{cm}^{-3}] = 2.1 \times A^{-0.37}$ with a correlation coefficient of $R = 0.58$. Comparing directly $v$ and $n$, we find that the density minimum is delayed for one day with respect to the velocity maximum ($\Delta t = -1$; Figure 4a). The corresponding power-law least-squares fit $n\ [\mathrm{cm}^{-3}] = 2 \times 10^6 \times v^{-2.1}\ [\mathrm{km\,s}^{-1}]$ is characterized by a high correlation coefficient of $R = 0.76$.

A similar equation holds for the magnetic field: For a 6-day lag one finds $B\ [\mathrm{nT}] = 2.8 \times A^{-0.26}$ with a correlation coefficient $R = 0.62$. Directly comparing $v$ and $B$ for our data gives for a 2-day delay $B\ [\mathrm{nT}] = 8540 \times v^{-1.2}\ [\mathrm{km\,s}^{-1}]$ with $R = 0.66$.

Finally, it should be emphasized that we repeated the whole procedure also for the complete C bin, E slice, and W slice, as well as for all three slices with the latitudinal domain

restricted to $\pm 30^\circ$ and the C bin restricted to $y = \pm 500$ and $y = \pm 700$ arcsec (see Section 2.2). The correlations for the C bin and complete E and W slices (appropriately lagged) are similar to those shown in Figure 5 for the M slice, having also comparable statistical significances. However, the restriction in the latitudinal range, *i.e.*, exclusion of high latitudes, significantly degrades the correlations and decreases their statistical significances.

## 4. Forecasting Procedure

The relationships presented in the previous section can be employed as a starting point in forecasting the solar wind parameters in periods of low CME activity. The straightforward application of the results presented in Figure 5 and the corresponding time lags would give a prediction with a minimum overall deviation (sum of differences squared) of the calculated ($C$) values from the observed ($O$) ones, since the procedure by definition relies on the least-squares procedure. However, applying such a procedure results in a significant underestimation of the perturbation amplitudes (*i.e.*, the peak values).[2] The reason why the "minimum-deviation forecast" cannot reproduce the amplitudes properly lies in the fact that the time lag between the CH "signal" $A(t)$ and the 1 AU response varies by $\pm 1$ day. Since both functions show sharp peaks, the 1-day lag between the observed and calculated peaks introduces a large $O - C$ difference, which gets smaller if the calculated peaks are smaller.

Since for space weather applications the basic interest lies in forecasting the amplitudes (peak values) of the solar wind fluctuations, as well as their durations, we certainly cannot be satisfied with the straightforward application of the least-square technique, which underestimates the amplitudes. So, instead of applying directly the relationships that would give the minimum-deviation forecast, we used these relationships only as a starting point in searching for more appropriate relationships that would reproduce properly the amplitudes of the investigated quantities. We call such relationships the "best forecast" option.

### 4.1. Forecasting the Solar Wind Parameters

In Table 2 we show our choice of the "best forecast" parameters for the solar wind quantities $v$, $n$, $T$, and $B$. The "predicted" values may be calculated by substituting the coefficients $c_0$ and $c_1$ given in Table 2 into the expression

$$f(t) = c_0 + c_1 A\left(t^*\right), \tag{1}$$

**Table 2** Coefficients used in the forecast equation $f(t) = c_0 + c_1 A(t^*)$, where $t^* = t - \Delta t$. The values of $\Delta t_{\mathrm{E}}$, $\Delta t_{\mathrm{M}}$, and $\Delta t_{\mathrm{W}}$ are time lags (expressed in days) for the E, M, and W slices, respectively.

| $f$ | $c_0$ | $c_1$ | $\Delta t_{\mathrm{E}}$ | $\Delta t_{\mathrm{M}}$ | $\Delta t_{\mathrm{W}}$ |
|---|---|---|---|---|---|
| $v$ [km s$^{-1}$] | 350 | 900 | 6 | 4 | 2 |
| $n$ [cm$^{-3}$] | 2 | 50 | 3 | 1 | −1 |
| $T$ [$10^3$ K] | 12 | 700 | 5 | 3 | 1 |
| $B$ [nT] | 3 | 25 | 4 | 2 | 0 |

[2]Note that Robbins, Henney, and Harvey (2006) applied in their forecast method the coefficients obtained by minimizing the mean of the absolute average fractional deviation of the calculated and observed values (see (2) therein). This is, to a certain degree, similar to applying the coefficients obtained by the least-squares fit.

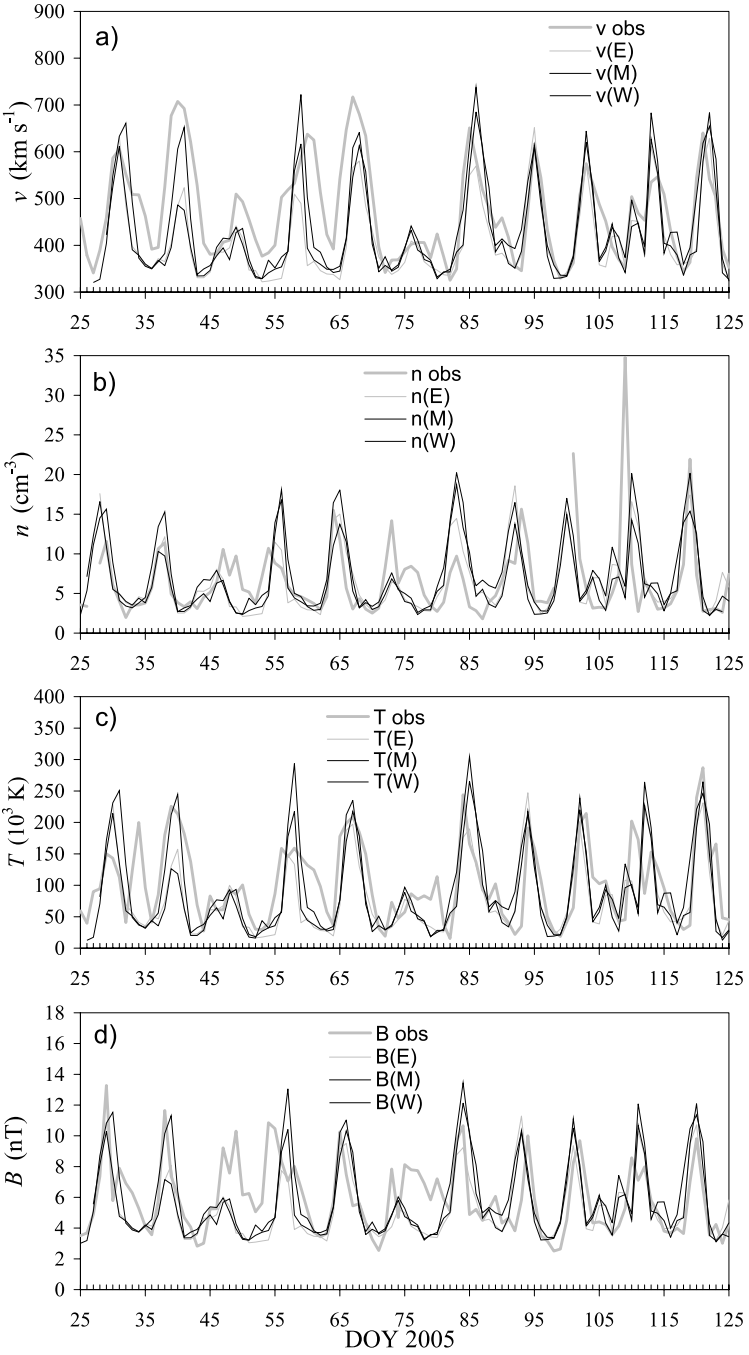


**Figure 6** Comparison of the calculated and the observed solar wind parameters in the period DOY 25 – 125: a) velocity; b) density; c) proton temperature; d) magnetic field strength. The observed data are drawn by gray bold lines; values "predicted" by using the E, M, and W slices are drawn by thin gray, thin black, and dashed black lines, respectively. In d) we also compare the sign of the $B_y$ GSE magnetic field component with the sign of the line-of-sight magnetic field in the coronal hole.

**Table 3** Relative difference between the calculated ($C$) and the observed ($O$) peak values ($\delta_{\%} = 100(O - C)/C$). The forecast is based on the M-slice data. The mean of absolute values $|\delta|$ is given in the last row.

| Peak | $\delta_n$ (%) | $\delta_B$ (%) | $\delta_T$ (%) | $\delta_v$ (%) |
|---|---|---|---|---|
| 1 | 17.14 | −47.78 | 16.67 | −6.89 |
| 2 | −3.63 | −56.00 | −63.04 | −38.09 |
| 3 | −51.42 | −87.27 | −21.95 | −14.68 |
| 4 | 43.68 | 6.09 | 36.40 | 2.74 |
| 5 | 13.89 | 6.36 | 11.44 | −12.38 |
| 6 | −118.46 | −54.29 | −14.67 | 5.80 |
| 7 | 52.68 | 12.65 | 9.96 | 4.69 |
| 8 | 13.33 | 9.09 | 19.07 | 3.29 |
| 9 | – | 11.82 | 9.32 | 10.03 |
| 10 | −104.12 | 18.10 | 9.01 | 11.94 |
| 11 | −9.50 | 18.33 | −8.71 | 5.04 |
| $\overline{\lvert\delta\rvert}_{\%}$ | 42.8 | 29.8 | 20.0 | 10.6 |

where $f$ stands for $v$, $n$, $T$, and $B$, whereas the retarded time $t^* = t - \Delta t$ is defined by the time lags $\Delta t$ determined in Section 3 and listed in Table 2. Note that there is a significant difference between the coefficients $c_0$ and $c_1$ displayed in Table 2 and those shown in the insets in Figure 5. Generally, the slopes ($c_1$) are roughly twice as steep in the "best forecast" option as in the least-square option.[3]

In Figure 6 we present for $v(t)$, $n(t)$, $T(t)$, and $B(t)$ the comparison between the calculated values (applying (1) and using the E-, M-, and W-slice data) with the observed data. The graphs show that the reliability of all three predictions is comparable, yet the W slice is the most accurate one. Inspecting the curves more carefully, we find that the predicted peak values of the daily solar wind parameters are generally quite close to the observed ones, especially in the case of the wind speed and temperature. It should be noted that predictions based on the latitude-restricted slices degrades the prediction accuracy.

Figure 6 demonstrates the limits of the proposed method of forecasting the CIR – HSS characteristics. In Table 3 we present the fractional differences, $\delta = (O - C)/C$, between the observed peak values, $O$, and the calculated peak values, $C$, evaluated using the M-slice data. We preferred to use the form $(O - C)/C$ instead of the more common form $(O - C)/O$, since in the forecasting situation only the $C$-value is known. Consequently, to predict how much the observed value might deviate from the calculated one, one has to know a typical deviation expressed in terms of $C$. In this respect let us note that the average $(O - C)/C$ and $(O - C)/O$ values do not differ significantly. The mean of absolute values $|\delta|$ is given in the last row of Table 3.

Inspecting Figure 6a, one finds that the solar wind speed can be predicted six days in advance by monitoring the E slice, or four days in advance by monitoring the M slice, with more or less similar accuracy. The highest accuracy is provided by employing the W-slice data, but at that time the Earth is already in the CIR – HSS environment.

Inspecting Table 3, one finds that the proposed forecasting method should be most successful in the case of the solar wind velocity. The last column of Table 3 shows that the

[3]Basically, the "best forecast" coefficients were determined by inspecting the data points in the upper-right part of the graphs in Figure 5 and the unperturbed ($A = 0$) values of the solar wind parameters. It should be noted that the chosen parameters are to a great deal provisional, but bearing in mind the intrinsic data scatter, there is no use in developing some strict method of determining these parameters.

deviation between the observed and calculated velocity peak values is smaller than 10% in 6 out of 11 peaks, and only one peak shows deviation larger than 15%. The average of the absolute values $|\delta|$ amounts to $\overline{|\delta|} \approx 10\%$. The RMS value of $O - C$ is 76 km s$^{-1}$, which is $\approx$13% of the mean $\overline{v} = 600$ km s$^{-1}$ (see the last row of Table 1). The time of the HSS velocity peak can be estimated to $\pm 1$ day. The final check of the prediction can be performed two days in advance by monitoring the W slice. Here, the prediction of $v$ has accuracy better than $\delta = \pm 10\%$.

The results shown in Table 3 demonstrate that in the case of the other three solar wind parameters, somewhat less reliable forecasts can be expected. The accuracy is lowest in the case of the density, where the RMS value amounts to 7.7 cm$^{-3}$, which represents almost 50% of the mean of the density peak values (see Table 1). The RMS value in the case of the magnetic field and the proton temperature amounts to 2.7 nT and $45 \times 10^3$ K (26% and 24% of the mean values of the magnetic field and temperature peaks, respectively). However, the accuracy of the peak time remains generally within $\pm 1$ day, similar to the case of the solar wind velocity.

In Figure 6d we indicate also the orientation of the solar wind magnetic field, by displaying the sign of the $B_y$ magnetic field component in the GSE coordinate system. The minus sign ($B_y < 0$) implies also that the magnetic field is directed toward the Sun ($B_x > 0$), whereas the plus sign ($B_y > 0$) corresponds to the field directed outward ($B_x < 0$). Comparing the orientation of the solar wind magnetic field with the magnetic polarity of the corresponding coronal hole (CH polarities being shown above the signs of $B_y$) we find that the orientation of the magnetic field in all CIR – HSSs is consistent with the CH polarities. This implies that the orientation of the magnetic field in a particular CIR – HSS may be predicted with great confidence by checking the polarity of the corresponding coronal hole. Obviously, this result is of great importance in predicting the geoeffectiveness of CIR – HSSs.

## 5. Discussion and Conclusion

In the presented analysis we focused on the amplitudes of CIR – HSS-associated variations of the daily values of the solar wind parameters $v$, $n$, $T$, and $B$ to establish the relationship with the position/area parameters of the related low-latitude coronal holes in the period of very low CME activity. The most important results of our study may be summarized as follows:

1. Time variations of physical parameters characterizing CIR – HSSs at 1 AU, as well as their amplitudes, are closely related to the area/position of CHs.
2. During periods of low CME activity the CIR – HSS-associated peak values of daily averaged solar wind parameters $v$, $T$, $n$, and $B$ can be predicted several days in advance.
3. The peak times can be predicted to within $\pm 1$ day in most of the cases.
4. The peaks appear in a sequence: density, magnetic field strength, temperature, velocity — the delays after the CH transit over the central meridian, on average, amount to 1, 2, 3, and 4 days, respectively.
5. The average accuracy in predicting the amplitude of the velocity peak is generally around 10%, whereas the amplitudes of $T$, $B$, and $n$ could be predicted, on average, to about 20%, 30%, and 40%, respectively.
6. If high latitudes are excluded, the correlations between $A$ and solar wind parameters degrade, indicating that high-latitude CHs contribute to the 1 AU CIR – HSS characteristics too.
7. The orientation of the magnetic field in a particular CIR – HSS can be predicted by inspecting the polarity of the corresponding coronal hole.

Our results regarding the solar wind speed are consistent with those presented by Robbins, Henney, and Harvey (2006), who used a 1/2-day time resolution and employed the CH areas based on Kitt Peak He I 1083-nm spectroheliograms. They found that, on average, the velocity peak appears 3.7 days after a low-latitude CH passes over the central meridian, whereas our data give a delay of 3.6 days (Table 1). Furthermore, their relationship $v = 330 + 930A$ is very close to the expression we propose, $v = 350 + 900A$ (see (1) and Table 2).

In the top panel of their Figure 5, Robbins, Henney, and Harvey (2006) compared the observed and "predicted" values of the solar wind speed for a 54-day interval in the declining stage of solar cycle 22. This interval is considered as good for forecasting, and the average $|O - C|/O$ difference is found to be around 10%. However, inspecting the peak values in the graph, one finds that during the two main HSS intervals the predicted peak values range around 550 km $s^{-1}$, whereas the observed speeds achieve values around 650 km $s^{-1}$. This gives a value of $|\delta|$ in the range 15 – 20% for two out of three velocity peaks present in the considered interval. In comparison, our procedure resulted in $|\delta| > 15\%$ only in one out of eleven peaks (see Table 3). Since our $v(A)$ forecasting expression is quite similar to the one used by Robbins, Henney, and Harvey (2006), this might indicate that the determination of the CH areas by using SXI data offers better predictions than by using He I 1083-nm spectroheliograms. However, to draw a definite conclusion, a direct comparison of the same time interval would be necessary, preferably covering various phases of solar cycle (*e.g.*, one method could be superior in one phase but inferior in another). A similar statement holds for the comparison with more sophisticated methods of solar wind forecasting that are based on magnetostatic potential field source surface modeling (*e.g.*, Arge and Pizzo, 2000; Arge *et al.*, 2004, and reference therein).

In this paper we extended the analysis also to the solar wind proton density, proton temperature, and the magnetic field strength, and we established expressions that provide forecasting of these parameters too. Furthermore, our results are based on the GOES-SXI CH measurements, which could be performed in real time, fully automatically. Consequently, our method may be used for developing a fully autonomous/automatic forecasting of the solar wind characteristics in periods of low solar activity.

Finally, we emphasize that the proposed forecasting method could be employed in real-time calculations of the Sun – Earth transit time of CMEs and shocks. The interplanetary propagation of CMEs is dominated by aerodynamic drag, decelerating fast ejections, or accelerating those that are slower than the solar wind (*e.g.*, Gopalswamy *et al.*, 2000; Vršnak and Gopalswamy, 2002; Vršnak *et al.*, 2004; Michalek *et al.*, 2004; Manoharan, 2006). The aerodynamic drag acceleration depends on the difference between the velocity of the CME and the ambient solar wind: $a = -\gamma(v_{\rm CME} - v_{\rm sw})|v_{\rm CME} - v_{\rm sw}|$, where $\gamma$ is proportional to the solar wind density (*e.g.*, Cargill, 2004; Vršnak *et al.*, 2004). Thus, it is expected that the solar wind speed and density both play an important role in the interplanetary kinematics of an ejection (for an observational indication of the CH – HSS effects on the motion of an ejection see Tappin, 2006).

For example, if a fast ejection moves through the space behind the stream interface (SI), where the wind velocity is high and the density is low, it will be decelerated much less than in the normal slow solar wind ambience. On the other hand, a slow ejection launched ahead of, and caught up by a HSS, would be accelerated more efficiently than in the normal slow wind, first due to the density enhancement ahead and around the SI, and then by the fast flow behind the SI. Such a scenario could explain at least a part of events showing the Sun – Earth transit times shorter than expected from the velocities measured by coronagraphs (*e.g.*, Michalek *et al.*, 2004).

The solar wind speed is also an essential parameter in models of the interplanetary shock propagation such as STOA or ISPM (for an overview see, *e.g.*, Dryer *et al.*, 2004; Smith, Dryer, and Fry, 2006, and references therein). Predictions of these models could be possibly improved by employing the forecasted solar wind speed instead of that measured at 1 AU at the time when the disturbance was launched.

**Acknowledgements** This work is sponsored by the Air Force Office of Scientific Research, USAF, under Grant No. FA8655-06-1-3036. M.T. acknowledges support by the Austrian Science Fund (FWF grant J2512-N02). We are grateful to the ACE, GOES-SXI, and SOHO-LASCO teams for their open data policies. We are thankful to the referee for constructive comments and suggestions that led to a significant improvement of the paper.

## References

Alves, M.V., Echer, E., Gonzalez, W.D.: 2006, *J. Geophys. Res.* **111**, A07S10.
Arge, C.N., Pizzo, V.J.: 2000, *J. Geophys. Res.* **105**, 10465.
Arge, C.N., Luhmann, J.G., Odstrčil, D., Schrijver, C.J., Li, Y.: 2004, *J. Atmos. Solar Terr. Phys.* **66**, 1295.
Borovsky, J.E., Denton, M.H.: 2006, *J. Geophys. Res.* **111**, A07S08.
Borovsky, J.E., Steinberg, J.T.: 2006, *J. Geophys. Res.* **111**, A07S09.
Brueckner, G.E., *et al.*: 1995, *Solar Phys.* **162**, 357.
Burlaga, L.F., Lepping, R.P.: 1977, *Planet. Space Sci.* **25**, 1151.
Cargill, P.J.: 2004, *Solar Phys.* **221**, 135.
Dal Lago, A., Gonzalez, W.D., de Gonzalez, A.L.C., Vieira, L.E.A.: 2002, *Adv. Space Res.* **30**, 2225.
Dal Lago, A., *et al.*: 2006, *J. Geophys. Res.* **111**, A07S14.
Detman, T., Smith, Z., Dryer, M., Fry, C.D., Arge, C.N., Pizzo, V.: 2006, *J. Geophys. Res.* **111**, A07102.
de Toma, G., Arge, C.: 2005, In: Sankarasubramanian, K., Penn, M., Pevtsov, A. (eds.) *Large-Scale Structures and Their Role in Solar Activity*, *Astron. Soc. Pacific Conf. Ser.* **346**, 251.
Dryer, M., Smith, Z., Fry, C.D., Sun, W., Deehr, C.S., Akasofu, S.-I.: 2004, *Space Weather*. **2**, S09001.
Gopalswamy, N., Lara, A., Lepping, R.P., Kaiser, M.L., Berdichevsky, D., St. Cyr, O.C.: 2000, *Geophys. Res. Lett.* **27**, 145.
Gosling, J.T., Pizzo, V.J.: 1999, *Space Sci. Rev.* **89**, 21.
Hill, S.M., *et al.*: 2005, *Solar Phys.* **226**, 255.
Jones, H.: 2005, In: Sankarasubramanian, K., Penn, M., Pevtsov, A. (eds.) *Large-Scale Structures and Their Role in Solar Activity*, *Astron. Soc. Pacific Conf. Ser.* **346**, 229.
Manoharan, P.K.: 2006, *Solar Phys.* **235**, 345.
McComas, D.J., Bame, S.J., Barker, P., Feldman, W.C., Phillips, J.L., Riley, P., Griffee, J.W.: 1998, *Space Sci. Rev.* **86**, 563.
Michalek, G., Gopalswamy, N., Lara, A., Manoharan, P.K.: 2004, *Astron. Astrophys.* **423**, 729.
Odstrčil, D., Pizzo, V.J., Arge, C.N.: 2005, *J. Geophys. Res.* **110**, A02106.
Odstrčil, D., Riley, P., Zhao, X.P.: 2004, *J. Geophys. Res.* **109**, A02116.
Pizzo, V.J., *et al.*: 2005, *Solar Phys.* **226**, 283.
Robbins, S., Henney, C.J., Harvey, J.W.: 2006, *Solar Phys.* **233**, 265.
Schwenn, R.: 2006, *Living Rev. Solar Phys.* **3**(2). http:////www.livingreviews.org/lrsp-2006-2.
Shen, C., Wang, Y., Ye, P., Wang, S.: 2006, *Astrophys. J.* **639**, 510.
Smith, C.W., L'Heureux, J., Ness, N.F., Acuna, M.H., Burlaga, L.F., Scheifele, J.: 1998, *Space Sci. Rev.* **86**, 613.
Smith, Z., Dryer, M., Fry, C.D.: 2006, *Space Weather*. **3**, S07002.
St. Cyr, O.C., Howard, R.A., Sheeley, N.R.: 2000, *J. Geophys. Res.* **105**, 18169.
Stone, E.C., Frandsen, A.M., Mewaldt, R.A., Christian, E.R., Margolies, D., Ormes, J.F., Snow, F.: 1998, *Space Sci. Rev.* **86**, 1.
Tappin, S.J.: 2006, *Solar Phys.* **233**, 233.
Tsurutani, B.T., Gonzalez, W.D.: 1987, *Planet. Space Sci.* **35**, 405.
Tsurutani, B.T., *et al.*: 2006, *J. Geophys. Res.* **111**, A07S01.
Vršnak, B., Gopalswamy, N.: 2002, *J. Geophys. Res.* **107**(A2), SSH2-1.
Vršnak, B., Ruždjak, D., Sudar, D., Gopalswamy, N.: 2004, *Astron. Astrophys.* **423**, 717.
Vršnak, B., Temmer, M., Veronig, A.M.: 2007, *Solar Phys.*, DOI 10.1007/s11207-007-0311-x.
Webb, D.F., *et al.*: 2000, *J. Geophys. Res.* **105**, 27251.
Xie, H., Gopalswamy, N., Manoharan, P.K., Lara, A., Yashiro, S., Lepri, S.: 2006, *J. Geophys. Res.* **111**, A01103.
Yashiro, S., Gopalswamy, N., Michalek, G., St. Cyr, O.C., Plunkett, S.P., Rich, N.B., Howard, R.A.: 2004, *J. Geophys. Res.* **109**, 7105.